RESEARCH ARTICLE
PLANETARY SCIENCES

Earth and Planetary Physics
8: 338–355, 2024
doi: 10.26464/epp2024008

Snow and regolith albedo variations using CRISM data at McMurdo crater, Mars

Sehajpal Singh*, and Deepak Singh

Centre of Studies in Resources Engineering, Indian Institute of Technology Bombay, Mumbai, India

Key Points:

- Surface albedo determination from imaging spectroscopy data.
- Maximum drop in mean albedo of snow-covered pixels is related to Mars Year 34.
- Dust deposition is transient and reversible, owing to the recovery of surface albedo after the global dust storm event.

Citation: Singh, S., and Singh, D. (2024). Snow and regolith albedo variations using CRISM data at McMurdo crater, Mars. *Earth Planet. Phys.*, *8*(2), 338–355. http://doi.org/10.26464/epp2024008

Abstract: The cryosphere component provides the most reliable and insightful indications of any planet's climate dynamics. Using data from the Compact Reconnaissance Imaging Spectrometer for Mars (CRISM), we develop a novel approach to determining the broadband Visible and Near Infrared (VNIR) albedo of the Martian surface. This study focuses on albedo changes in the McMurdo crater, part of Mars's south polar layer deposits. We compare seasonal and interannual variations of the McMurdo surface albedo before, during, and after the Global Dust Storm (GDS) of Martian Year (MY) 34. As the seasons progressed from spring to summer, the mean albedo in MY 32 and 34 plunged by over 40%, by about 35% in MY 33, and by slightly more than 30% in MY 35. Compared interannually, however, *mean* albedo values *within* both seasons (spring and summer) exhibited no significant differences in those same years. Notably, interannual albedo difference maps reveal albedo variation of more than ±0.3 in certain regions of the crater. Considering only snow-covered pixels, interannual albedo differences suggest that Mars dust had a pervasive impact on Mars's cryosphere. Variations in maximum and minimum albedo values as high as 0.5 were observed, depending upon differences in the dust levels in Martian snow/ice. The maximum and the minimum snow albedo values were lowest in MY 34, indicating the effect of the intense dust storm event that year. The average snow albedo decreased from 0.45 in MY 32 to 0.40 in MY 33 and to 0.33 in MY 34, and then rose back to 0.40 in MY 35. This trajectory suggests a temporary deposition of dust, partially reversed after the GDS by self-cleaning mechanisms (local aeolian process and CO_2 sublimation/deposition cycle).

Keywords: Mars; Martian ice; albedo; dust storm; Mars surface; Martian climate

1. Introduction

The cryosphere component is the most sensitive and informative indicator of a planet's climate variations. Albedo changes affect a planet's energy budget and trigger climate activity (Fenton et al., 2007). Studying cryosphere and albedo changes on parts of Mars can provide insights into local energy exchanges and contributions towards the energy budget of the red planet. Telescopic observations of Mars dating back to the early 19th century have revealed albedo changes on the planet (de Vaucouleurs, 1954). Modern satellites have demonstrated that changes in the global albedo patterns, which were once assumed to be driven by vegetation (Pollack et al., 1967), are instead the result of the unrelenting redistribution of sand and dust by the Martian winds (Geissler et al., 2016). Global albedo monitoring was initiated in the 1970s with the Viking Orbiter Infrared Thermal Mapper (IRTM) and has continued, based on images from cameras onboard the Hubble Space Telescope (HST) and the Mars Global Surveyor (MGS), Mars Odyssey, Mars Express, and Mars Reconnaissance Orbiter (MRO) spacecraft. These images have recorded a large number of instances of regional albedo feature variations (Kieffer et al., 1977; Thomas and Veverka, 1979; Christensen, 1988; Herkenhoff and Murray, 1990; Bell III et al., 1999; Szwast et al., 2006; Cantor et al., 2010; Martínez et al., 2012; Vincendon et al., 2015; Geissler et al., 2016; Rice et al., 2018; Bapst et al., 2022).

According to various studies, Mars's surface area has brightened or darkened by at least 10% (Geissler, 2005; Szwast et al., 2006) between the Viking and MGS eras. Mars's surface either undergoes periodic changes during large-scale dust storms or changes gradually over many years. Changes in surface albedo occur primarily during the storm season as a result of isolated events (Vincendon et al., 2015). The albedos of polar caps on Mars, too, play a crucial role in the dynamics of the planet's atmosphere and surface (Cantor et al., 2010). Indeed, modeling studies show that only a few microns of dust can modify snow albedo by tens of percent (Titus et al., 2003; Singh and Flanner, 2016; Khuller et al., 2021).

Correspondence to: S. Singh, sehajpunjabi@gmail.com
Received 10 AUG 2023; Accepted 11 DEC 2023.
First Published online 30 JAN 2024.

Because much of the surface of Mars can be categorized as cryosphere (polar and near-polar regions), the deposition of small amounts of dust can alter the planet's total surface albedo significantly. Good correlations exist between short-term variations in the albedo at different wavelengths, the magnitudes of variability decreasing with increased wavelength. Storm-related dust deposition on the polar cap has obvious potential to modify the polar surface's albedo and, in turn, the polar region's heat budget (Cantor et al., 2010). In all these studies, local/regional or global dust storms have indeed been found to play a vital role in altering the surface albedo. Studies mentioned above have detected inter-annual and seasonal albedo changes (global coverage) with spatial resolution of hundreds or thousands of meters for both polar and non-polar regions. How these albedo changes affect wind patterns, dust activity, and the feedback between these processes and the Martian climate, however, remain active areas of research (Fenton et al., 2007). Albedo changes in the south polar region of Mars are an intriguing topic of study. Some of the research gaps that need to be addressed are (but are not limited to):

(1) Identifying and characterizing specific albedo features,

(2) Determining primary drivers or mechanisms that lead to albedo changes,

(3) Iinvestigating feedback processes between albedo changes and local or regional climate dynamics, and

(4) Examining the relationships between albedo and volatile ices (particularly carbon dioxide and water ice).

The Martian south pole has a large ice cap composed of water ice and carbon dioxide ice, with the latter dominating the region (Kieffer, 1979; Kieffer et al., 2000; Titus et al., 2003; Bibring et al., 2004; Montmessin et al., 2007). By monitoring changes in albedo, we can study alterations in the polar ice cap's size, extent, and growth or retreat; these can be linked to the redistribution of water between the atmosphere and surface and subsurface reservoirs. These observations provide valuable insights into Mars's climate and long-term weather patterns, further deepening our knowledge of its past and present climate dynamics. Due to its tilted axis, Mars undergoes major seasonal fluctuations analogous to those on Earth. Interannual and seasonal processes of changes in ice distribution can be examined by keeping an eye on changes in albedo at the South Pole (James et al., 2001; Calvin et al., 2017). For instance, the South Pole's carbon dioxide ice cover goes through repetitive cycles of expansion and retreat. These changes impact weather patterns, winds, and atmospheric dynamics. Albedo monitoring helps in tracking these processes, furthering our understanding of Mars's seasonal climate variations. Albedo measurements provide information about the polar ice caps' composition, stability, and changes, data essential to mission planning, especially resource utilisation and risk assessment (Langevin et al., 2007). Mars dust storms may significantly alter the planet's surface's albedo (reflectivity). The South Polar Cap's albedo drops when dust is deposited on it (Kieffer, 1979; Kieffer et al., 2000), affecting the temperature of the polar cap. Thus, albedo monitoring can advance our insights into how dust storms alter the energy balance and/or thermal properties of the south-polar region, not to mention the entire planet.

Global dust storms (GDSs) on Mars are sporadic phenomena occurring approximately every 3–5 MYs from combinations of regional and local dust-lifting events (Smith et al., 2002; Haberle et al., 2017). Most GDSs have appeared to initiate in the southern hemisphere near perihelion, though some (GDSs of MY 25 and MY 34) have been associated with the Mars equinox (Wolkenberg et al., 2020). Compared to other storms, the GDS in MY 34 (MY 1 began at L_s = 0 on April 11, 1955; Clancy et al., 2000) exhibited a decay constant two and a half times faster than average (Wolkenberg et al., 2020). Since radiative heating by dust triggers a GDS, higher insolation in the southern as compared to the northern hemisphere may be considered the reason for the inception of a GDS in the southern hemisphere (Sánchez-Lavega et al., 2019). Unlike most of the previous GDSs, the MY 34 GDS is unique — the first of all observed regional dust storms that developed in Acidalia Planitia to evolve into a GDS, the first GDS observed to initiate from the northern hemisphere (Sánchez-Lavega et al., 2019). Though Sánchez-Lavega suggested that the GDS of MY 34 (2018) penetrated the southern polar cap region, dust coverage was not observed to occupy the full south polar cap (Hernández-Bernal et al., 2019). A satisfactory understanding of polar dynamics during this major dust storm event remains lacking; hence, we try to use an alternative approach to study the reflective behavior of the south polar cap during this mega dust storm.

Some possible precursor dust storms to the MY 34 GDS have been identified, notably over the Hellas region and the southern polar cap edge region (Wolkenberg et al., 2020). Thus, we focus on the McMurdo crater (84.4°S, 0.9°E), located at the margin of the "south polar layered deposits" (SPLDs) of Planum Australe, Mars (Figure 1). The crater was named after the McMurdo Station in Antarctica (see Gazetteer of Planetary Nomenclature). The crater is chosen for this study as it is near to the edge of the cap, lower in elevation, and therefore more exposed to storms than the center of the cap. The crater, 23 km in diameter, lies in the Mare Australe quadrangle of Mars. Most of the crater is entrenched beneath the south polar cap, which is thought to have formed only 10 Ma ago (Herkenhoff and Plaut, 2000), making it relatively recent. McMurdo crater is the largest crater in the surface of this SPLD region; the impact that created it pierced through a portion roughly 1500 meters in thickness (Schaller et al., 2005). Tanaka et al. (2014) mapped this unit as an Amazonian polar undivided unit (Apu unit), an ice-rich layered plateau (commonly referred to as a "polar layered deposit", PLD).

The aim of our work is to advance our understanding of how the unusual GDS of MY 34 affected the South polar region of Mars; we do so by studying in considerable detail the observable surface albedo changes in the McMurdo crater region. Through this study, we try to understand the seasonal and inter-annual variations in albedo within this part of the south polar cap of Mars. We investigate spatiotemporal changes in albedo patterns due to deposition and sublimation of volatile ices, such as carbon dioxide and water ice. We also consider the role of another primary driver of albedo change — Mars dust, which impacts the reflective properties of the surface. Hence, we provide a novel approach, using imaging spectroscopy to determine broadband albedo changes (interannual and seasonal) at moderate spatial resolution, and comparing

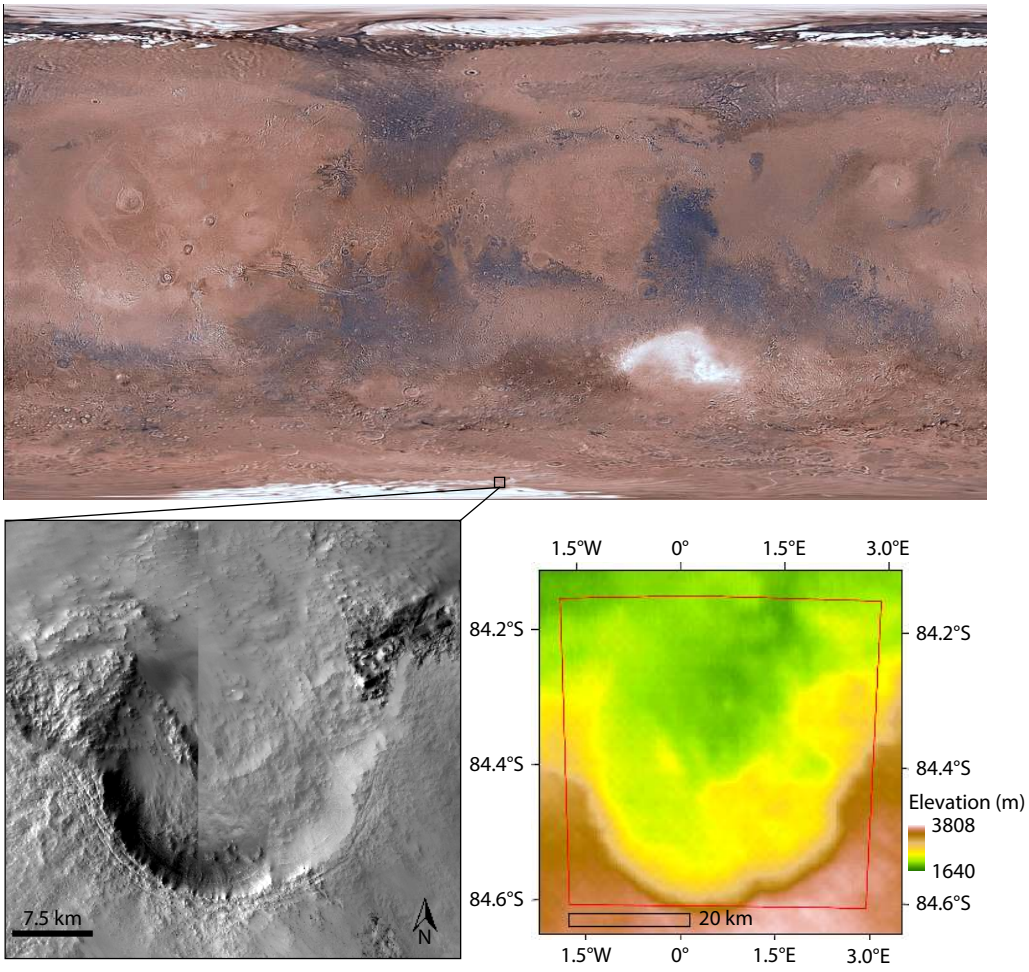

Figure 1. (Top) Location of McMurdo crater represented by black square on Mars Viking Colorized Global Mosaic (Credits: NASA AMES /USGS). (Bottom left) Magnified view of McMurdo crater as seen in Thermal Emission Imaging System (THEMIS) DAY IR 100 m Global Mosaic v13.4 product (Edwards et al., 2011). (Bottom right) HRSC-MOLA blended DEM at 200 m per pixel of the McMurdo crater region.

albedo maps created before and after MY34 GDS. The impact of dust, generated by local or global dust storms, on the planet's cryosphere must be addressed to understand Martian climate change better. We use the terms 'snow' and 'ice' interchangeably throughout this paper.

This paper is organized as follows. In Section 2, we discuss the spacecraft and the instrument that provide our data, along with which observations of our study region we chose to examine. Section 3 focuses on the methodology adopted to pre-process the data, and highlights the method developed to calculate the broadband albedo using data from the Compact Reconnaissance Imaging Spectrometer for Mars (CRISM) (Murchie et al., 2007). In Section 4, we present our findings of seasonal and interannual albedo changes, pre- and post-GDS albedo variations, and differences in snow albedo, and discuss them in detail. Finally, we summarize the study in Section 5.

2. Dataset: Spacecraft, Instrumentation and Observations

2.1 CRISM Instrument

Since November 2006, the Mars Reconnaissance Orbiter (MRO) has been carrying out observations from a near-circular (250 × 315 km), low altitude, near-polar orbit, with an ascending node positioned near 3 p.m. local mean solar time on the planet's dayside (Zurek and Smrekar, 2007). The visible-infrared hyperspectral mapper CRISM has studied the atmosphere and mapped the geology, composition, and layering of surface features on Mars. In addition to its primary objectives, CRISM's scientific goals were to explore seasonal processes on Mars and to search for surface albedo changes. CRISM measured reflectance at a spectral sampling of up to 6.5 nm with two detectors — Visible and Near Infrared (VNIR) or "S" detector (up to 107 channels, 0.36 to 1.05 μm) and Infrared (IR) "L" detector (up to 438 channels, 1.0–3.93 μm) — and imaged the surface with varying spatial resolution from as fine as 18 m per pixel down to 200 m per pixel, depending upon the observation modes. Each detector registered 480 pixels in the spectral dimension and 640 in the spatial dimension. Due to the failure of its thermoelectric coolers, CRISM L data collection ceased as of February 15, 2018; thereafter, CRISM acquired data in VNIR-only modes — Hyperspectral VNIR (HSV) and Multispectral VNIR (MSV). On April 3, 2023, NASA switched off CRISM permanently after having extended its mission by more than a decade.

2.2 CRISM Observations over the South Polar Cap (SPC)

Since CRISM was an imaging spectrometer that observed the planet through reflected solar radiation, it was well suited for spring and summer observations of the polar regions. The polar areas cannot be monitored during polar autumn and winter when the Sun does not irradiate them. The Sun starts rising at the Southern Pole near $L_s = 180°$, CRISM observations of the region are available only after $L_s = 180°$ and up to $L_s = 360°$. Another advantage of considering observations for $L_s = 180°$ to 360° is that this period corresponds to a "high dust loading season" (Kahre et al., 2017), making the effects of the MY 34 GDS more prominent. The CRISM observations used in this study belong to four Mars years, from MY 32 at L_s = 206.4°, to MY 35 at L_s = 325.9°, corresponding to October 2, 2014, and December 5, 2020, respectively. In order to reduce shadowing and significant phase effects, our study is focused primarily on near-nadir data (emergence angles lower than 10°) acquired with incidence angles lower than 75°. Nevertheless, a few observations with higher incidence angles are also used as low-quality data. In this paper, we study the impact of MY 34 (2018) GDS by monitoring albedo changes over the McMurdo crater region (Figure 1) using CRISM VNIR-only observations. The details of the observations used in this study are provided in Table S1.

3. Method

3.1 Pre-processing with CAT

We use CAT v7.4 (CRISM Analysis Toolkit, Version 7.4) plug-in to ENVI to preprocess the CRISM data. CRISM Targeted Reduced Data Records (TRDR, Version 3) *I/F* products data were acquired from Planetary Data System (PDS) Geoscience Node (https://ode.rsl.wustl.edu/mars/). *I/F* is defined as the recorded spectral radiance divided by the spectral radiance of the Sun at Mars distance at the time of observation. All PDS datasets had to be converted to CAT datasets, a format supported by the CAT toolkit. Apparent reflectance (R) from the *I/F* data is retrieved by dividing with the cosine of the incidence angle. We get the solar incidence angle for each pixel at aeroid from the respective Data Derived Record (DDR) file obtained from PDS.

$$R = \frac{I/F}{\cos i},$$

where i is the solar incidence angle — 0° when the Sun is overhead and 90° at the horizon.

The Lambertian ($\cos i$) photometric correction assumes the simplest surface bidirectional reflectance function; it corrects the data to a normal illumination geometry. This allows observations acquired at different incidence angles to be more readily compared. No atmospheric corrections were performed because the S-detector observations are not affected by the Mars atmosphere (Morgan et al., 2009) since much of the Martian atmosphere is composed of CO_2 (Leighton and Murray, 1966), which has negligible absorption in VNIR. A DDR file accompanies each observation pointed at Mars's surface. It is required to map project data calibrated to radiance or *I/F* units, or to process these data further to Lambert albedo, corrected for photometric, atmospheric, and thermal effects. Geometric information from DDRs is used to georeference the CRISM cubes. Before projecting the sensor space, two VNIR summary products are generated — TRU (enhanced true color representation) and RBR (Red Blue Ratio). The detailed descriptions and formulation for these summary products are provided in the work of Viviano et al. (2014). Spectral parameter sensor space data are flattened to attain column-wise smoothening before assigning them projection using DDR files. All these summary products are in a polar stereographic-projected coordinate system (the origin of the coordinate system is the south pole — 90°S, 0°E).

3.2 Integrating CRISM Wavelengths to Derive VNIR Broadband Albedo

After pre-processing, the geo-referenced CRISM cube is transformed into a raster in which each pixel value represents band-averaged values of albedo (hereafter termed "broadband VNIR albedo" or just albedo). These values are weighted with solar spectral irradiance calculations (from Labs and Neckel, 1968). These weights are based on the amount of energy available for each wavelength. We developed a python code (using Geospatial Data Abstraction Library) to convert the projected CRISM observations to these raster files. Each pixel of the raster represents the broadband albedo, represented by the following equation:

$$\text{Broadband Albedo} = \frac{w_1R_1 + w_2R_2 + w_3R_3 \cdots + w_nR_n}{(w_1 + w_2 + w_3 + \cdots + w_n)},$$

where w_n = flux weightage of nth band, R_n = apparent reflectance of nth band.

Flux weightage of the nearest wavelength band was assigned in cases for which exact CRISM wavelength band information was not available. These raster files were then imported into ArcGIS software for further analysis; interannual and seasonal mosaics were prepared from these raster datasets and CRISM VNIR summary products (Viviano et al., 2014), as discussed in the next section. All these raster files have spatial reference as stereographic south pole projections with 32-bit float pixel type; cell size is 200 m. 'Maximum' mosaicking method is used to mosaic overlapping areas; that is, the output cell value of the overlapping areas of raster dataset will be the maximum value of the overlapping cells. The maximum mosaicking operator has been used to enhance the albedo of icy surfaces.

3.3 Mapping Snow Using CRISM VNIR-only Wavelengths

As mentioned in Section 2.1, the CRISM instrument ran in VNIR-only mode (0.4–1.05 m) after 2017 due to loss of the CRISM cryocooling system. Thus, the conventional approach of detecting and differentiating water ice or dry ice by analyzing absorption bands could not be followed. Therefore, we attempt to map ice using CRISM VNIR wavelengths as explained by Viviano et al. (2022). An RBR summary product was generated for each CRISM observation with help of the CAT toolkit. These products were imported into ArcGIS, and interannual and seasonal mosaics were generated. A mask of RBR ≤ 3 was used to distinguish ice from soil (Viviano et al., 2022). Hence, a 'minimum' mosaicking operator is used to mosaic overlapping regions, implying that the output cell value of overlapping areas of the raster dataset will be the minimum value of the overlapping cells. Using this mask, we generate

albedo maps of only snow-covered regions of the crater, which is discussed in Section 4.6.

The aforementioned steps have been illustrated in the form of a flowchart (Figure 2) for better clarity.

4. Results and Discussion

4.1 VNIR CRISM Observations: Seasonal Surface Changes

Variation in part of the South polar residual cap can be observed in TRU summary products of the McMurdo crater. Each row of Figure 3 depicts the seasonal change from spring to summer (left to right) for a particular Martian year. Figures 3a, 3c, 3e, and 3g show, respectively, true-color CRISM S-detector observations collected in the spring seasons (L_s = 180° to 270°) of MYs 32, 33, 34, and 35. Figures 3b, 3d, 3f, and 3h correspond to summer season (L_s = 270° to 360°) observations recorded in MYs 32, 33, 34, and 35, respectively. In the spring season observations, Martian ice in image strips acquired at lower L_s values appears less reflective than in those taken at higher L_s values, mainly due to newly deposited dust over the icy region. The effect of this dust decreases as the spring season progresses (solar longitude increases): for MY 34 (Figure 3e), the mean albedo value in observation MSV00049BAB_01 (~215.6°, see Table S1 for details) is 0.36, compared to 0.43 in observation MSV0004A490_01 (~235.3°, see Table S1 for details); similarly, for MY 35 (Figure 3g): mean albedo is 0.36 in observation MSV000532E1_01 (~205.2°, see Table S1 for details) compared to 0.45 for observation MSV00054A7B_07 (~266.6°, see Table S1 for details).

Summer season (L_s = 270°–360°) images (Figures 3b, 3d, 3f, and 3h) are clearer; a sharp visible boundary of the ice extent can be seen (except in Figure 3b, MY 32, for which too few CRISM observations were available). Because these images include not just ice or mixtures of ice and dust, but also water ice clouds or haze and dust in the atmosphere, using them to interpret surface processes is difficult. Nevertheless, our visual interpretation of each row (left to right), suggests that atmospheric dust settles as southern summer approaches. Other studies, also, have shown that near L_s = 250° in the south polar region the dust returns to climatologically typical levels of dust optical depths (Smith, 2019; Guzewich et al., 2020). For all MYs 32–35, the ice cover falls drastically as the seasons progress and is confined to the central mound of the crater. Between L_s 270° to 360°, little or no ice is visible on the equator-facing wall of the crater, as it remains sunlit throughout the southern spring and summer.

4.2 VNIR CRISM Observations: Interannual Surface Changes

In MY 34, local dust storms were prevalent during L_s = 180° to 270° (spring season or dust storm season) mainly over the Hellas region and the southern polar cap edge (Sánchez-Lavega et al., 2019; Wolkenberg et al., 2020). The effect can also be observed by visual interpretations (Figure 3e). Yearly variations of the snow, mixed or covered with dust, were observed during the spring season (column 1 of Figure 3). To account for the effects of Martian dust after settling from the atmosphere, CRISM observations made later than L_s = 200° are considered for this study. These observa-

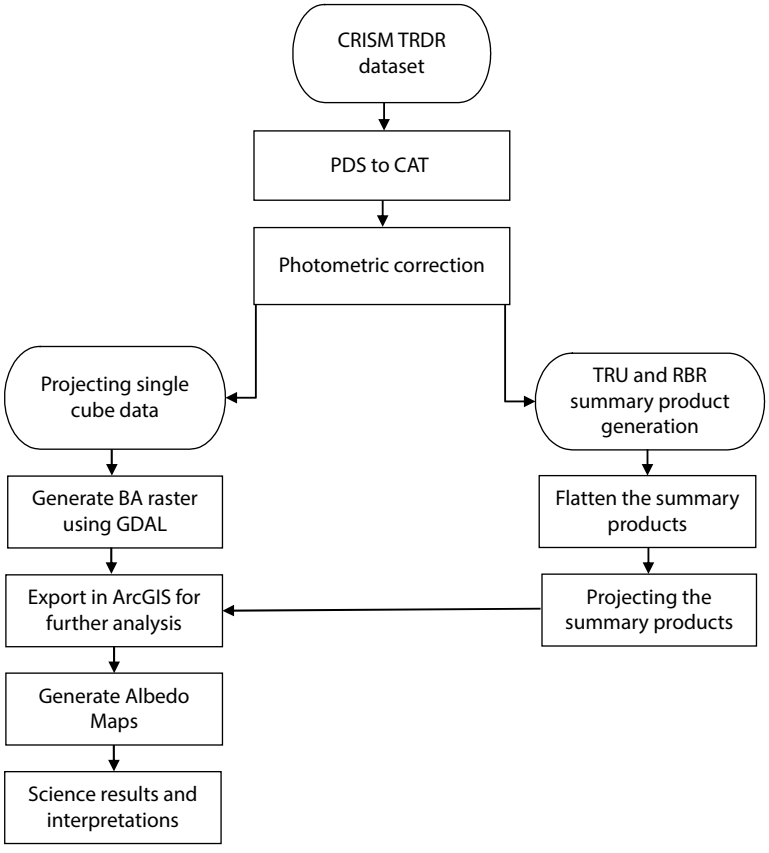

Figure 2. Flowchart of methodology for processing and analyzing CRISM VNIR-only observations.

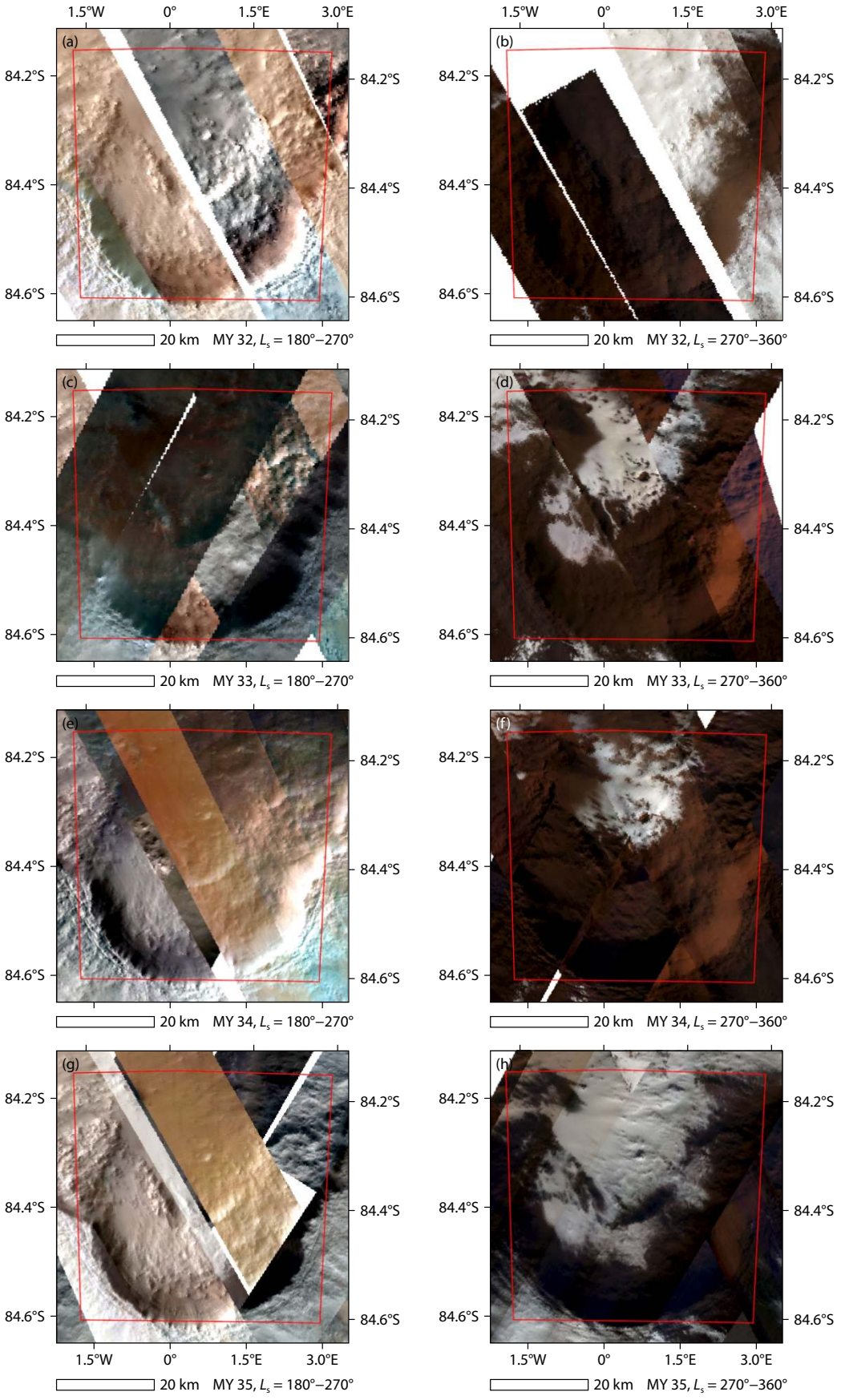

Figure 3. True Color Mosaics of McMurdo crater, part of the south polar cap. The first row represents MY 32; rows 2–4 represent MYs 33 to 35. Column 1 indicates observations from the Southern spring (L_S: 180° to 270°). Column 2 presents Summer observations (L_S: 270° to 360°).

tions indicate that the dust storm season of MY 34 was more intense than in the other years of this study (see Section 4.5 for more details), obscuring a clear view of the entire crater surface.

Column 2 of Figure 3 illustrates the inter-annual changes in the extent of snow cover in McMurdo crater during the four summer seasons (L_s = 270° to 360°) included in this study (layers in the images are ordered such that maximum snow/ice cover is visible). The VNIR CRISM observations for MY 32, 33, 34, and 35 for the summer season (L_s = 270°–360°) are shown in Figures 3b, 3d, 3f, and 3h, respectively. (Insufficient S-detector CRISM observations are available for MY 32.) Ice is visible in only two CRISM observations (passing through the North-Eastern extent of the crater) belonging to the beginning of summer (L_s = 270° to 280), while the other two observations are of mid-summer (L_s = 300° to 320°). Ice is concentrated mainly in the central region of the crater, with little or no ice on the equator-facing wall of the crater throughout the summer season. The minimal ice content seen in MY 34 (Figure 3f) is attributed to the fact that the only available image is from late summertime (L_s = 311° to 330°) CRISM observations, in contrast to the CRISM observations (L_s = 280° to 330°) used for MY 33 and 35.

4.3 Broadband VNIR Albedo Maps: Seasonal Changes

A uniform trend appears in the seasonal changes in VNIR albedos observed over these four years. Each row of Figure 4 depicts the seasonal changes in albedo from spring to summer (left to right) for a particular Martian year. We observe significant changes in albedo patterns as the season changes from spring to summer. We notice a noticeable decrease in the VNIR albedo of the crater region. While the spring season is dominated by high albedo values (greater than 0.36) of dusty ice, the non-icy or barren regolith's lower albedo values (0.08–0.36) eclipse the surface. As the season progressed from spring to summer in the southern hemisphere of Mars, the crater's mean albedo dropped by over forty percent in MY 32 and MY 34, by about thirty-five percent in MY 33, and by slightly more than thirty percent in MY 35 (see Table 1 for details).

Maximum albedo values also fell in all four years during the transition from spring to summer. Noticeable declines were observed in MYs 32, 33, 34 and 35, as follows: from 0.78 to 0.60; 0.72 to 0.63; 0.65 to 0.58; and 0.73 to 0.60, respectively. Our results (Table 1) also indicate that the *mean* albedo value each spring was higher than the summer mean, which is in agreement with the observations of James et al. (2005), Paige and Ingersoll (1985). These observations suggest that the higher insolation during spring brightens up the seasonal frost, and that sublimation of CO_2 frost deposits are probably the cause of albedo decreases into summer (James et al., 2001). The much higher dust storm intensity in MY 34 probably explains why the greatest decrease in the VNIR albedo was observed in that year (Wolkenberg et al., 2020); the minimum values corresponding to non-icy pixels also plunged, that year, hinting at thinning or removal of dust cover over the Martian regolith, due to increase in solar longitude.

4.4 Broadband VNIR Albedo Maps: Interannual Changes

Figure 4 shows maps of maximum broadband albedo in the crater region. To help understand and interpret interannual surface albedo changes within the region, we have divided the VNIR albedo values into six categories, color-coded by albedo strength. Figures 4a, 4c, 4e, and 4g are, respectively, the broadband albedo maps for the spring or dust storm seasons (L_s= 180° to 270°) of MY 32, 33, 34, and 35. The mosaic of Figure 4e indicates that, during the MY 34 (2018) GDS, the majority of the McMurdo crater had maximum albedo values lying between 0.37 and 0.50, with only small regions outside the south-western rim having albedo values greater than 0.50.

Numbers of pixels representing VNIR albedo values greater than 0.50 in the McMurdo region during the southern spring were highest in MY 32 (Figure 4a), followed by MY 35 (Figure 4g) and MY 33 (Figure 4c). Of all four Martian years, the fewest pixels with albedo values of 0.50 or higher were recorded in MY 34, a consequence of the higher dust-storm activity during MY 34; from 0.78 in MY 32, the maximum albedo value in the McMurdo region dropped to 0.72 in MY 33 and then fell to 0.65 in MY 34 before restabilizing to 0.73 in MY 35 (see Table 1 for details). The higher maximum albedo observed in MY 32 compared to MY 33 is probably an artifact of the difference in time of acquisition of CRISM observations between those years. Thus, we interpret the change from MY 32 to MY 33 to be insignificant compared to the drop from MY 33 to MY 34, which we attribute to the impact of the MY 34 GDS on snow albedo.

However, *mean* albedo values were more similar for all four years, being 0.48, 0.42, 0.41, and 0.45 for MYs 32, 33, 34, and 35, respectively. The mean albedo of the crater did not show any considerable decrease because the global dust storm enhanced the brightness of non-icy regolith even while causing an opposite effect on the frost/ice.

Surprising trends were noticed in *minimum* albedo values of the crater, which declined from 0.26 in MY 32 to 0.18 in MY 33 to 0.17 in MY 35, but with an abrupt increase to 0.30 in MY 34. These counterintuitive observations can be explained by assuming that the deposition of bright fresh dust increases the albedo of non-icy Martian regolith as the dust particles scatter and reflect the sunlight, reducing the amount of solar radiation absorbed by the surface.

Column 2 of Figure 4 depicts summer season (L_s= 270° to 360°) changes in VNIR albedo values for MY 32 (Figure 4b), MY 33 (Figure 4d), MY 34 (Figure 4f) and MY 35 (Figure 4h). Changes in albedo can be observed due to variations in snow cover within the crater (see Figure 3 for comparison). However, summer changes are not as prominent as those during the spring season. Minimum albedo values remain almost unaltered, hovering near 0.10. These values correspond to the known minimum albedo of the non-icy dust-free surfaces. The maximum albedo of 0.58, observed in MY 34, shows a minor deviation from 0.60 in MY 32 and MY 35 and 0.63 in MY 33. The mean albedo of 0.31 for MY 35 was slightly higher than that of the other years (0.28 in MY 32, 0.27 in MY 33, and 0.24 in MY 34) due to consideration of early summer observations for MY 35 than in the other years, because of limited availability of data.

In both spring and summer, maximum and mean albedo values declined from MY 32 to MY 34 and recovered in MY 35 (Table 1).

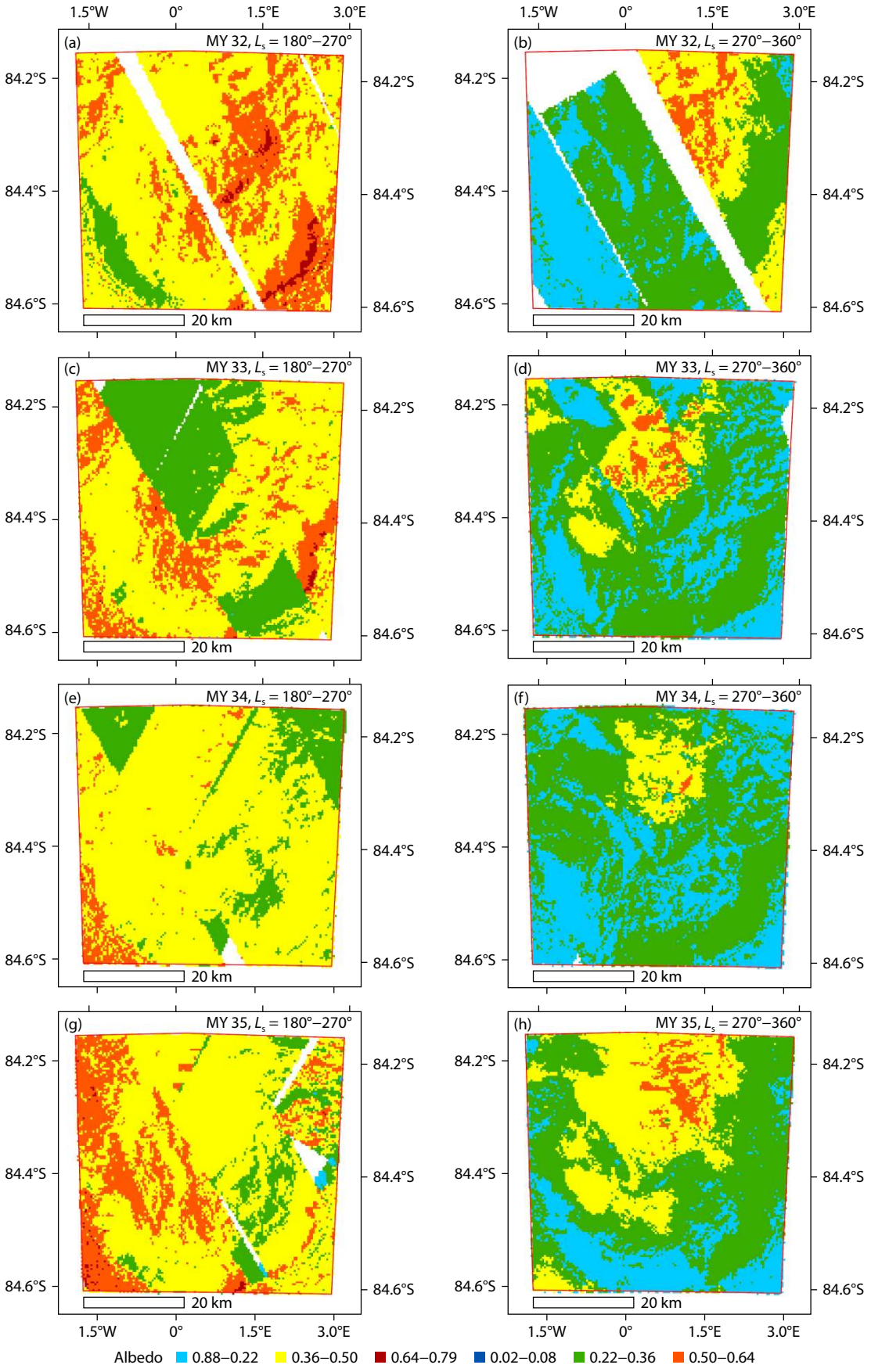

Figure 4. Broadband VNIR maps showing maximum albedo values at McMurdo crater. The first row represents MY 32; rows 2–4 represent MYs 33–35. Column 1 indicates observations from the Southern spring (L_S: 180° to 270°). Column 2 presents summer observations (L_S: 270° to 360°).

Table 1. VNIR albedo values of McMurdo crater region during the span of four Mars years (MY 32–35).

MY	VNIR albedo of McMurdo crater						VNIR albedo of only ice-covered region of crater		
	Maximum		Mean		Minimum		Maximum	Mean	Minimum
	Spring	Summer	Spring	Summer	Spring	Summer	Summer		
32	0.78	0.60	0.48	0.28	0.26	0.08	0.60	0.45	0.21
33	0.72	0.63	0.42	0.27	0.18	0.08	0.63	0.40	0.14
34	0.65	0.58	0.41	0.24	0.30	0.10	0.58	0.33	0.12
35	0.73	0.60	0.45	0.31	0.17	0.13	0.60	0.40	0.17

But minimum albedo values are different. The abrupt rise in minimum albedo value in the spring of MY 34 is explained by the interaction of fine bright dust with the Martian surface, increasing the albedo of bare surfaces (Fenton et al., 2007).

It is to be noted that pure H_2O snow has a slightly higher albedo than CO_2 snow at visible wavelengths, but the near-infrared (NIR) albedo of CO_2 snow is higher than that of water snow (Warren et al., 1990; Singh and Flanner, 2016). Thus, the broadband albedo of pure CO_2 ice is relatively higher than that of H_2O ice. In Figure 4, the VNIR albedo of snow falls into two categories (represented by yellow and orange shades) for all four Martian years. We believe that such differences are due to variations in dust content in ice and not differences in albedos of dry ice and water ice. If these differences were due to the two different types of ice, then the yellow region's extent would be less than that of the orange region, as dry ice is perennial and found in abundance near the Southern pole of Mars (Kieffer, 1979). If changes had been due to the appearance/disappearance of CO_2 ice, then they would be evident during the transition from spring to summer season. Also, mixtures of dust with CO_2 and H_2O ices have similar albedo values (Singh and Flanner, 2016); thus, these two ices cannot be differentiated based only on albedo values.

4.5 Interannual Albedo Difference Maps

Apart from seasonal trends at distinct wavelengths in polar regions, albedo values can vary with storm activity near the vicinity of the cap (James et al., 2007; Malin et al., 2008; Cantor et al., 2010), and with variation in the grain sizes of ice particles (Langevin et al., 2005, 2007). Figure 5 presents mosaic maps showing albedo differences arrived at by subtracting values recorded one year in our study period (MY 32–35) from those recorded in the same season of a different year. The pairs of years chosen are ones comparing pre- and post-GDS observations; these comparisons reveal albedo changes of more than ±0.3 in certain regions. These variations greatly exceed those reported by Vincendon et al. (2015), based on observations related to the MY 28 GDS; they found albedo changes (extremities) of just ±0.04. We attribute the higher variation in albedo values in our observations to differences in the deposition and sublimation of Martian ices, on varying temporal and spatial scales near the south pole of Mars.

Figure 5a, in which we compare the albedo distribution in the spring season of MY 32, two years pre-GDS, with that of the GDS year MY 34, reveals noticeable changes (both brightening and darkening). Most of the region's albedo *plummeted* (–0.10 to –0.20) during MY 34, compared to MY 32, due to the large amount of GDS atmospheric dust in MY 34; but the MY 34 albedo of the southwestern rim of the crater *rose* by approximately the same factor. A comparison of summer albedo distributions of these two years (Figure 5b) reveals a somewhat similar scenario, the principal difference being that summer albedo values in much of the region were not significantly different between the two years; the similarity is that the eastern side of the crater shows a drop in albedo in MY 34, compared to MY 32, but the central portion's albedo increases. We interpret these summer differences as due to effects of dust on icy and non-icy surface, respectively. The mean albedo difference values (MY 32 values–MY 34 values) were found to be +0.06 and +0.04 for the southern spring and summer, respectively.

For certain subregions, the VNIR albedo values detected in MY 33, one year prior to the GDS year MY 34, were also greater than those observed in MY 34 (Figures 5c and 5d), but not as much greater as in MY 32. Note: Owing to differences in the solar longitude of the available observations used in our comparisons and usage of a few observations belonging to low-quality data (mentioned in Section 2.2), we cannot rule out the possibility that negative values of albedo difference (MY 33–MY 34) also occurred (see green region in Figure 5c).The mean values for albedo difference (MY 33–MY 34) were found to be +0.01 and +0.027 for the southern spring and summer, respectively. This indicates that there was not as much difference in albedo values between MY 33 (pre-GDS year) and MY 34 as between values recorded in MY 32 (pre-GDS year) and MY 34 (GDS year), suggesting a gradual transition in effectivity of atmospheric dust as the GDS year approached.

Color-coding in all rows is as follows: Areas in which albedo values were higher by 0.20 or more in the reference year than in the GDS year MY 34 (or, in the case of the fourth row, higher in post-GDS MY 35 than in pre-GDS MY 33) are in red; areas in green are those where albedos in the reference year were lower by 0.20 or more, than in the GDS MY 34 (or, in case of 4th row, lower in post-GDS MY 35 than in pre-GDS MY 33). Areas in which albedo values changed less than +/–0.20 are shown in yellow. The left column presents differences in albedo observed in Mars's southern spring (L_s: 180° to 270°); the right column represents differences between the two years' observations in the Mars summer (L_s: 270° to 360°).

Comparing the immediate post-GDS year (MY 35) to the GDS year (MY 34), we see significant improvement in albedo, especially in the summer season: compared to the mean albedo difference of +0.04 (Figure 5e) between their spring seasons, the summer

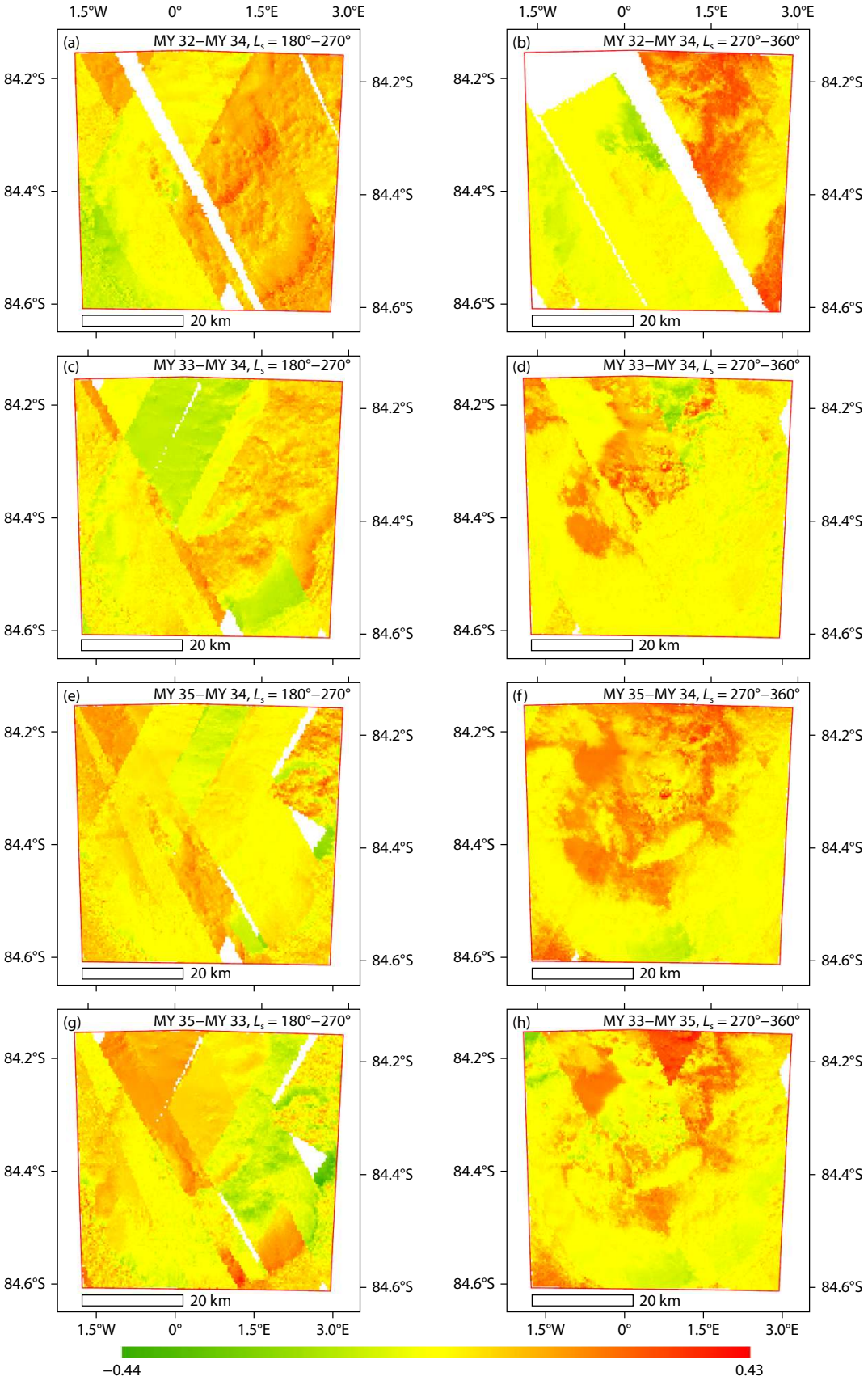

Figure 5. Mosaic interannual albedo-difference maps (McMurdo crater). First row: maps of MY 32 albedo values minus MY 34 values; second row: MY 33–MY 34; third row: MY 35–MY 34. These first three rows present differences between albedo values in pre- and post-GDS years to values in the same season of the GDS year MY 34; regions showing positive differences were dimmed in MY 34, relative to the pre- or post-GDS reference year. The fourth row, MY 35–MY 33 compares albedo values one year after the GDS to values one year before the GDS.

season mean difference was found to be +0.07 (Figure 5f). Most pixels represented an increase in albedo by around 0.20 to 0.30 (shades of red in Figure 5f) from the summer of MY 34 to the summer of MY 35. The yellow-colored region represents no significant difference in the albedo values for the two years. All these observations suggest that the dust storm in MY 34 was more intense and responsible for considerable albedo changes, far more than any previously studied global dust storm, in agreement with the observations of Wolkenberg et al. (2020) that dust opacities of the cores of storms in MY 28 and MY 34 were larger than 1.75 and 1.90, respectively, while the maximum dust opacity in MY 34 exceeded 2.1 (the largest value observed during any GDS of the past two decades), when the retrievals were binned. Comparisons of albedo data collected in the immediate pre- and post-GDS years (MY 35–MY 33, Figures 5g and 5h) provide clear evidence that the albedo of a major part of the crater hadn't stabilized even a year after the GDS event. The mean value of the albedo difference between MY 35 and MY 33 was found to be +0.02 in the spring season and +0.04 in the summer. Note: We did not compare the post-GDS year MY 35 with the pre-GDS year MY 32 because CRISM coverage in MY 32 was insufficient.

4.6 Snow Albedo Changes

Mosaicking of all red blue ratio (RBR) summary products was done in a manner similar to that used to prepare the VNIR albedo raster dataset (see Section 3.1), but with the mosaicking operator being used as 'minimum' instead of 'maximum'. This was done to enhance the effect of ices present on the surface: a mask of RBR ≤ 3 was used to differentiate ice from soil (Figure 6, orange-red color region). The snow extent can be verified visually by comparing Figures 3 and 6. We observed that this RBR mask detects ice reliably only in the summer season (L_s: 270° to 360°); in spring, RBR summary products saturate (Column 1, Figure 6) and thus cannot distinguish ice from other reflective surfaces. Icy soil cannot be differentiated from dust/soil in the VNIR, as they can be in the Shortwave Infrared (SWIR) region (Viviano et al., 2022). It is also obvious that the maximum RBR value during the summer season (Column 2, Figure 6) should be higher than that during spring (Column 1, Figure 6) as most of the ice gets sublimated during high solar insolation.

After determining the extent of summer months' snow cover in each of the four Mars years in this study, we analyzed interannual albedo changes of just the snow-covered portions of the crater region (Figure 7). Though most of the atmospheric dust settles after the summer solstice (L_s= 270°), the effect of the GDS was observed to continue even during the summer season. The maximum (and minimum) albedos of regional snow/ice in MYs 32, 33, 34 and 35 were found to be, respectively, 0.60 (0.21), 0.63 (0.14), 0.58 (0.12) and 0.60 (0.17) (see Table 1 for details). The variations in maximum and minimum values can be attributed to the amount of impurities (dust) present in the snow. Observing these maxima and minima, it can be deduced that Mars dust can reduce snow albedo by up to 0.49 or 75% (depending on the amount of dust content). The maximum and the minimum snow albedo values were the lowest in MY 34, the year of the especially-intense dust storm event. A GDS brings substantial amount of dust, which gets mixed with ices present near the poles, and alters the polar albedo. The albedo drop in MY 34 indicates an increase in dust particles deposited on the frozen surfaces, because dust has a lower reflectivity than the underlying icy surface.

The mean snow albedo dropped from 0.45 in MY 32 to 0.40 in MY 33, and on down to 0.33 in MY 34, before rising again to 0.40 in MY 35 (Figure 8). This sequence suggests that the intensity of the dust storm in MY 34 was significantly greater than that of the regional dust storms that occur every Mars year during the southern hemisphere spring; it also indicates that the dust deposition was temporary and reversible. This drop and rise of VNIR albedo values by roughly equal amounts (of about 17.5% from MY 33 to 35) highlights the significance of albedo as a factor in the energy balance of icy Martian surfaces. The surface was able to shed or remove the deposited dust through self-cleaning mechanisms, viz. aeolian processes and/or sublimation. Wind erosion and sublimation can thus remove or mitigate the impact of dust deposition over time.

The occurrences of dust storms and subsequent recovery of albedo exhibit a seasonal pattern. The correlations between dust storms and the albedo values of Martian icy surfaces indicate a link between atmospheric processes and the energy balance of the system. The demonstrated fact that Martian dust storms can temporarily alter the reflective properties of the Martian surface has significant implications for the local climate and energy budget.

We hypothesize that local aeolian processes and CO_2 sublimation/deposition cycle could be responsible for the removal of excess dust from the surface. This could lead to the recovery of the surface albedo to levels seen a few years prior to a GDS. However, further analysis and investigation are necessary to understand the specific mechanisms and processes involved in the recovery of albedo after a dust storm.

4.7 Ice-free Region Albedo Changes

Similar to the snow-covered portions of the crater region, noticeable variations in albedo were detected in the ice-free surface during the southern summer season. Figure 9 illustrates variations in albedo in non-icy portions of McMurdo crater in the four MY summers. While the minimum (and maximum) albedo values were similar in MYs 32 to 35, the *mean* albedo value (~0.44) for the year MY 34 (GDS year) was almost twice the mean albedo values of 0.22 (MY 32) and 0.23 (MY 33 and MY 35) in non-GDS years. This relatively higher value of mean albedo is possibly due to the presence of deposited Martian dust, as most of the dust generated during the GDS event settled, at around L_s = 250° (see Section 4.1). Dust storms have the ability to re-distribute existing surface dust, perhaps creating a more uniform layer. Even though the dust is made up of small, weakly reflective particles, a uniform layer of dust could result in a higher albedo than an uneven distribution of dust. Again, in this study the effect of Martian GDS dust was observed to be temporary, as the mean albedo rebounded to 0.23 in the summer of MY 35. Dust storms can deposit a transitory layer of fine dust particles on the surface, blanketing the rocks and Martian regolith. This layer of dust appears to be able to increase the overall reflectivity of the surface, contributing to a relatively higher albedo.

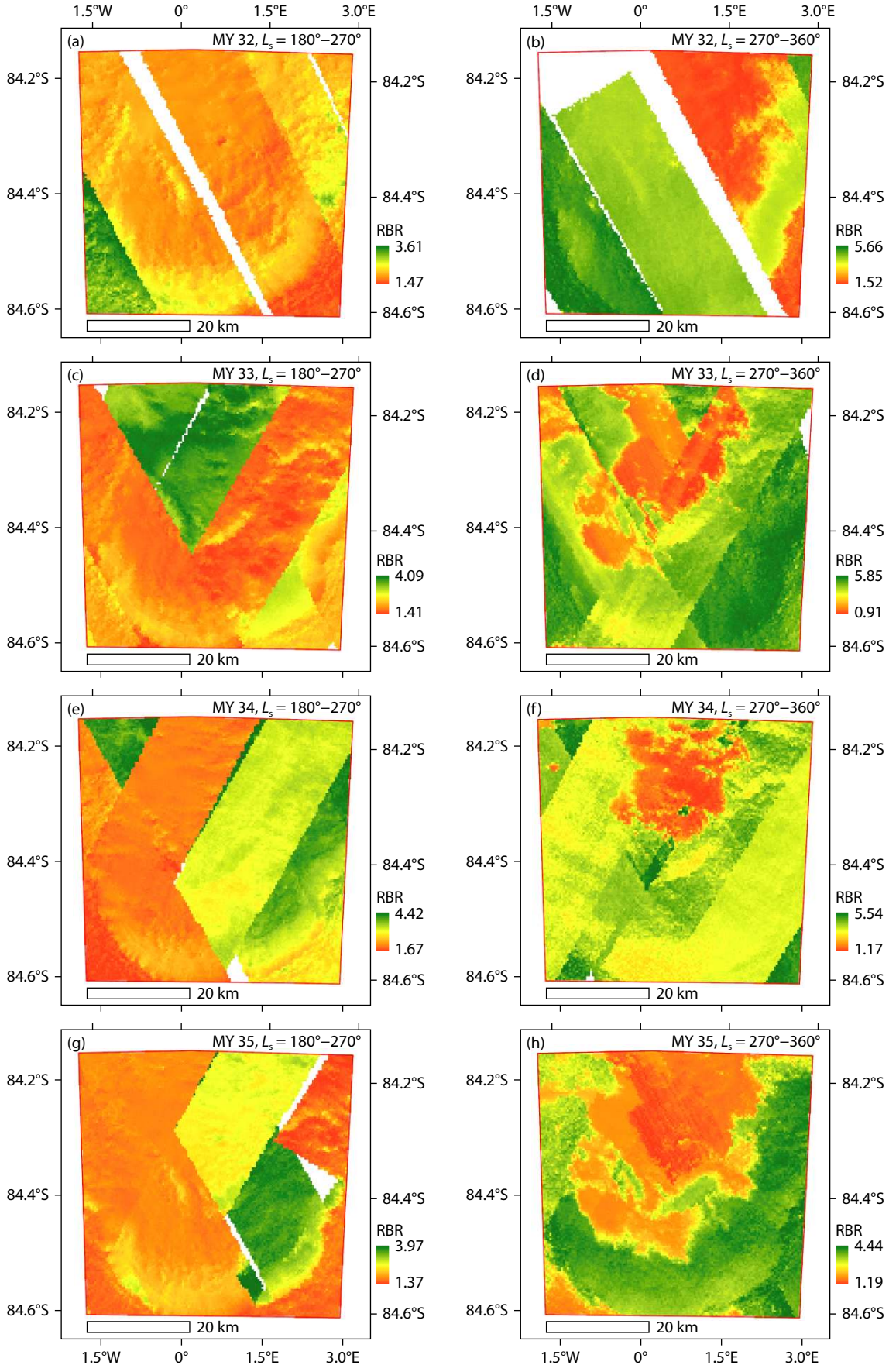

Figure 6. RBR maps of the McMurdo crater for the concerned period. Rows 1 to 4 represent MYs 32 to 35, respectively. Column 1 indicates observations made during the southern spring (L_s: 180° to 270°); summer observations (L_s: 270° to 360°) are indicated in Column 2.

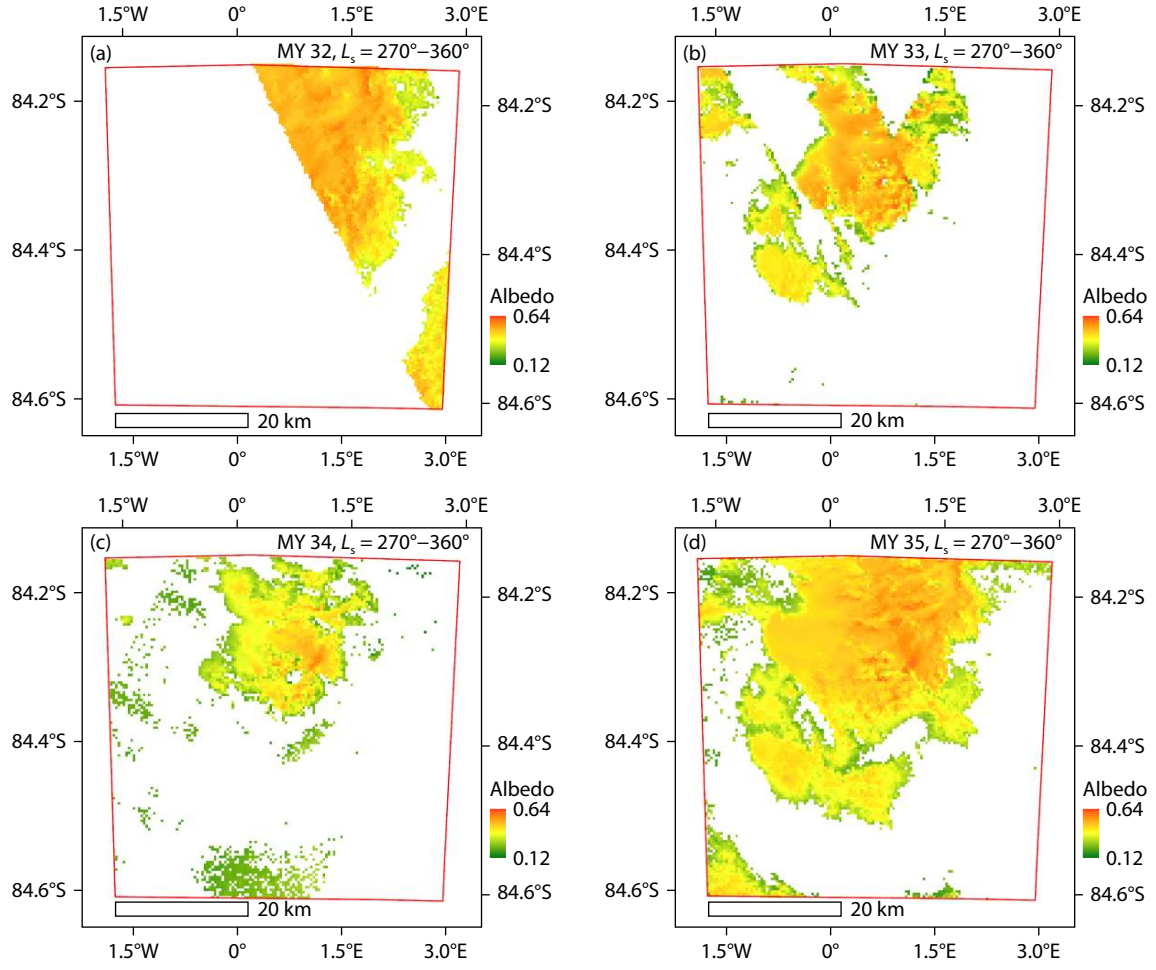

Figure 7. Variation of VNIR albedo of snow-covered pixels as observed in (a) MY 32, (b) MY 33, (c) MY 34 and (d) MY 35 during the Martian southern summer season (L_s: 270° to 360°).

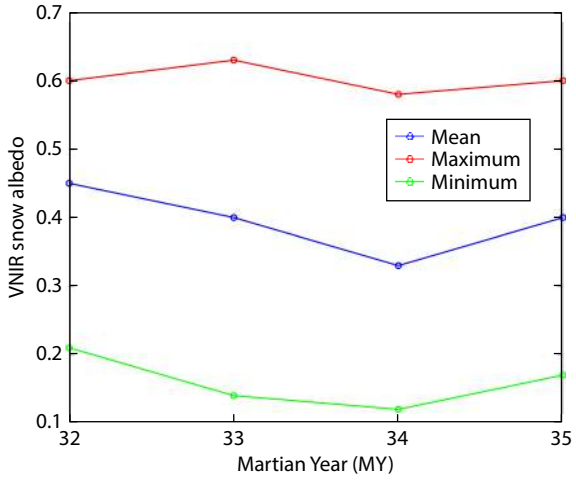

Figure 8. This graph shows the interannual variation in VNIR broadband albedo values of only snow-covered pixels during the southern summer season (L_s: 270°–360°).

5. Conclusions

We utilized CRISM data to calculate hemispheric albedo values on the southern surface of Mars at moderate spatial resolution. In this study, we have detected spatial and temporal changes (brightening and darkening) in surface albedo. As per previous studies (Christensen, 1988; Cantor, 2007; Kinch et al., 2007), we confirm that while dust lowered the albedo of the ice-covered region, the non-icy regolith area brightened up due to deposition of micrometer-sized dust particles. In most cases, the shape of the underlying surface can still be perceived, leading to the conclusion that even an optically thin layer of dust can alter the albedo of the surface. Though the albedo changes are seasonal, observations made in an especially intense global dust storm year, MY 34, reveal that its storm may have had a multi-year effect on the heat balance of the polar cap. The maximum drop in albedo was related to the MY 34 GDS. The maximum values of VNIR albedo were approximately 0.75, in concurrence with the results of Paige and Ingersoll (1985), who obtained south polar cap planetary albedos of 0.55–0.75, averaging about 0.65 over the entire Martian spring and summer seasons. The albedo difference maps reveal significant changes in specific areas of the crater.

Even the limited amount of storm dust that reached the McMurdo crater (which is southward of 80°S) during the MY 34 (2018) intense GDS (Hernández-Bernal et al., 2019) appears to have caused significant differences in the crater's albedo values between pre- and post-GDS observations. Mean albedo values in the McMurdo crater were found to be lowest in MY 34 of the four years studied, implying that the dust storm in MY34 was particularly

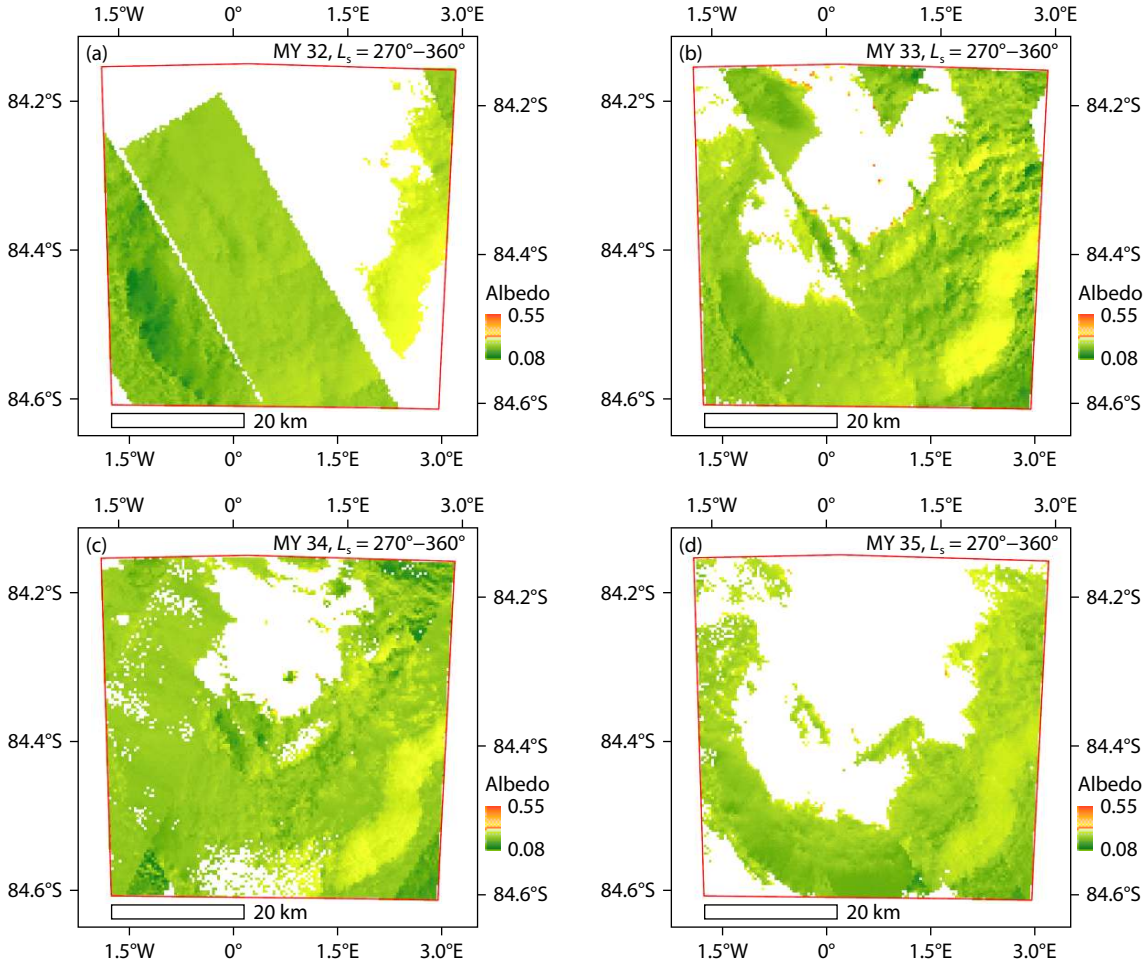

Figure 9. Variation of VNIR albedo of ice-free portions of the crater region, as observed in (a) MY 32, (b) MY 33, (c) MY 34 and (d) MY 35 for the Martian southern summer season (L_s: 270° to 360°).

intense, and responsible for significant albedo changes in the entire south polar region, corroborating noteworthy dust activities observed by Wolkenberg et al. (2020). In the following year, snow albedo values recovered to values observed in the immediately pre-dust activity years. The fact that the drop in mean albedo value from MY 33 to MY 34 was equal (17.5%) to the rise seen from MY 34 to MY 35 highlights the albedo's importance in maintaining the icy surface's energy balance. Interestingly, very similar results are observed for the non-icy region, where the much greater (91.3%) mean albedo drop and rise were again equal. The transient and reversible dust deposition could possibly be the result of self-cleaning mechanisms, viz. sublimation deposition cycles of CO_2 ice and/or aeolian processes.

The Martian south polar region's surface albedo variations have several implications in the context of climate change and/or understanding Mars's climate system. Albedo variations in non-dust storm seasons may be caused by changing configurations (layering and mixing) of two different types of ice — H_2O and CO_2 ice (Singh and Flanner, 2016). Sublimation and deposition of these volatile ices into water vapor and carbon-dioxide gas affect the Martian water cycle and CO_2 cycle, respectively. This in turn alters the pressure cycle, cloud formation, and other radiative and thermodynamical processes in the Martian climate system. Albedo variations could impact the stability of polar ice, thereby affecting possible future in-situ water resources. The polar ice caps, including the south polar region, partially sublimate during Martian summers. The rate at which this sublimation takes place can be impacted by changes in albedo, which thus influences the Martian atmosphere and surface temperatures, impacting the planet's climate feedback mechanisms. Studying such impacts on wind patterns, dust storms, and transport of gases is beyond the scope of this work.

Continuous monitoring of polar regions with high-resolution data will allow for the observation of more profound spatiotemporal albedo variations and enhance our comprehension of the responses of Mars's cryosphere to various atmospheric phenomena. We suggest that further efforts to address how CRISM VNIR datasets can be exploited to map ices on Mars's surface, especially observations taken during the spring in the planet's southern and northern hemispheres, could be of great value. Ice compositions can also be derived by studying surface temperatures from available thermal data; these observations will improve future comparative studies. Overall, cryosphere and albedo changes at the south pole of Mars are complex dynamic processes driven by a combination of seasonal and annual variations in temperature, atmospheric pressure, and solar radiation. Further research is needed

to better understand these processes and their impact on the Martian polar heat budget.

Acknowledgments

The authors acknowledge support from the Indian Institute of Technology Bombay (IITB) for providing the necessary facility and IITB seed grant. We acknowledge the efforts of the PDS Geoscience Node team (https://pds-geosciences.wustl.edu/) for making the CRISM data publicly available through the Mars Orbital Data Explorer (https://ode.rsl.wustl.edu/mars/).

Supplementary Materials

The following table lists details of all the CRISM images used in this study.

Table S1. Details of CRSIM observations considered of McMurdo crater from MYs 32–35.

S No.	Image ID	Obs. Time (Earth)	Season in SH	MY	L_s	Incidence angle (*i*)	Emission angle (*e*)
1	MSV00032F46_01	02-10-2014	Spring	32	206.4	79.58	0.26
2	HSV00033FCA_07	01-12-2014	Spring	32	243.7	65.26	0.26
3	HSV00034180_05	06-12-2014	Spring	32	246.9	68.40	0.26
4	HSV000341CF_07	07-12-2014	Spring	32	247.5	65.22	0.28
5	MSV0003431F_01	12-12-2014	Spring	32	250.7	66.02	0.44
6	HSV00034F29_01	14-01-2015	Summer	32	271.6	64.27	1.09
7	MSV000351F5_01	25-01-2015	Summer	32	278.4	64.06	0.96
8	HSV000357DB_01	22-02-2015	Summer	32	295.6	64.55	0.29
9	HSV00035C80_05	09-03-2015	Summer	32	304.6	70.53	0.28
10	HSV0003633D_01	06-04-2015	Summer	32	320.8	73.27	1.44
11	HSV0003E6D4_01	06-09-2016	Spring	33	217.4	71.64	0.30
12	HSV0003E7B3_07	09-09-2016	Spring	33	219.2	79.94	0.26
13	MSV0003E902_01	12-09-2016	Spring	33	221.2	73.65	8.87
14	HSV0003E984_01	14-09-2016	Spring	33	222.3	78.20	0.26
15	HSV0003E9DE_01	15-09-2016	Spring	33	223	78.19	0.23
16	HSV0003EAC5_03	17-09-2016	Spring	33	224.2	71.59	0.33
17	HSV0003F3E7_01	25-10-2016	Spring	33	248.2	65.67	0.21
18	HSV0003F5E7_01	29-10-2016	Spring	33	250.7	74.69	0.13
19	HSV00040C1B_05	31-12-2016	Summer	33	290.2	67.39	0.28
20	MSV000411AD_01	17-01-2017	Summer	33	300.4	67.23	1.24
21	HSV000412F1_01	20-01-2017	Summer	33	302.2	74.62	0.28
22	MSV00041428_01	24-01-2017	Summer	33	304.6	66.65	7.52
23	MSV000416CA_01	01-02-2017	Summer	33	309.3	69.10	8.65
24	HSV00041C67_05	25-02-2017	Summer	33	323.1	70.25	0.44
25	MSV0004200A_01	10-03-2017	Summer	33	330.3	76.63	13.85
26	MSV00049959_01	12-07-2018	Spring	34	209.4	74.79	0.31
27	MSV00049A7B_01	17-07-2018	Spring	34	212.5	74.73	0.30
28	MSV00049BAB_01	22-07-2018	Spring	34	215.6	75.01	0.29
29	MSV00049D06_01	28-07-2018	Spring	34	219.3	70.35	0.65
30	MSV0004A0D7_01	10-08-2018	Spring	34	227.3	74.73	0.18
31	MSV0004A490_01	23-08-2018	Spring	34	235.3	68.22	0.32
32	MSV0004A676_01	28-08-2018	Spring	34	238.7	67.92	0.24
33	MSV0004A9A1_01	06-09-2018	Spring	34	244.4	74.59	0.26
34	MSV0004C07A_03	24-12-2018	Summer	34	311.7	74.57	0.26
35	HSV0004C170_05	27-12-2018	Summer	34	313.4	70.25	0.27
36	MSV0004C249_01	29-12-2018	Summer	34	314.5	78.82	0.25

Continued from Table S1

S No.	Image ID	Obs. Time (Earth)	Season in SH	MY	L_s	Incidence angle (i)	Emission angle (e)
37	MSV0004C342_01	01-01-2019	Summer	34	316.3	66.07	1.63
38	MSV0004C566_05	07-01-2019	Summer	34	319.7	70.27	0.29
39	MSV0004C72D_03	12-01-2019	Summer	34	322.5	74.54	0.27
40	HSV0004C860_01	15-01-2019	Summer	34	324.2	83.26	0.24
41	MSV0004CB86_01	26-01-2019	Summer	34	330.3	81.29	0.28
42	MSV0004CC47_01	28-01-2019	Summer	34	331.4	79.49	0.28
43	MSV000532E1_01	22-05-2020	Spring	35	205.2	79.97	2.40
44	MSV00053BB3_03	03-07-2020	Spring	35	231.1	74.65	0.27
45	MSV00053E9A_07	16-07-2020	Spring	35	239.3	66.11	0.34
46	MSV0005420E_03	30-07-2020	Spring	35	248.2	71.56	0.25
47	MSV000543AF_01	05-08-2020	Spring	35	252	74.45	0.31
48	MSV00054870_03	21-08-2020	Spring	35	262.1	71.37	0.29
49	MSV00054941_01	24-08-2020	Spring	35	264	64.95	9.33
50	MSV00054A7B_07	28-08-2020	Spring	35	266.6	64.30	0.27
51	MSV000551A8_05	22-09-2020	Summer	35	282.2	70.76	0.26
52	MSV000552EC_03	27-09-2020	Summer	35	285.3	70.60	0.29
53	MSV000553D9_07	30-09-2020	Summer	35	287.1	63.28	0.29
54	MSV000554A6_03	02-10-2020	Summer	35	288.4	71.13	0.44
55	MSV00055665_03	07-10-2020	Summer	35	291.4	71.00	0.28
56	MSV000556BD_03	08-10-2020	Summer	35	292	70.97	0.27
57	MSV00055E8A_01	01-11-2020	Summer	35	306.4	69.53	0.33
58	MSV00056214_03	12-11-2020	Summer	35	312.8	70.74	0.32
59	MSV000566B3_01	27-11-2020	Summer	35	321.4	73.69	4.35
60	MSV0005690B_01	05-12-2020	Summer	35	325.9	82.58	0.28

References

Bapst, J., Piqueux, S., Edwards, C. S., Wolfe, C., Hayne, P. O., Kass, D. M., and Kleinböhl, A. (2022). Surface dust redistribution on Mars from interannual differences in temperature and albedo. *J. Geophys. Res.: Planets*, *127*(12), e2022JE007365. https://doi.org/10.1029/2022JE007365

Bell III, J. F., Wolff, M. J., Daley, T. C., Crisp, D., James, P. B., Lee, S. W., Trauger, J. T., and Evans, R. W. (1999). Near-infrared imaging of Mars from HST: Surface reflectance, photometric properties, and implications for MOLA data. *Icarus*, *138*(1), 25–35. https://doi.org/10.1006/icar.1998.6057

Bibring, J. P., Langevin, Y., Poulet, F., Gendrin, A., Gondet, B., Berthé, M., Soufflot, A., Drossart, P., Combes, M., …the OMEGA Team. (2004). Perennial water ice identified in the south polar cap of Mars. *Nature*, *428*(6983), 627–630. https://doi.org/10.1038/nature02461

Calvin, W. M., Cantor, B. A., and James, P. B. (2017). Interannual and seasonal changes in the south seasonal polar cap of Mars: Observations from MY 28-31 using MARCI. *Icarus*, *292*, 144–153. https://doi.org/10.1016/j.icarus.2017.01.010

Cantor, B. A. (2007). MOC observations of the 2001 Mars planet-encircling dust storm. *Icarus*, *186*(1), 60–96. https://doi.org/10.1016/j.icarus.2006.08.019

Cantor, B. A., James, P. B., and Calvin, W. M. (2010). MARCI and MOC observations of the atmosphere and surface cap in the north polar region of Mars. *Icarus*, *208*(1), 61–81. https://doi.org/10.1016/j.icarus.2010.01.032

Christensen, P. R. (1988). Global albedo variations on Mars: Implications for active aeolian transport, deposition, and erosion. *J. Geophys. Res.: Solid Earth*, *93*(B7), 7611–7624. https://doi.org/10.1029/JB093iB07p07611

Clancy, R. T., Sandor, B. J., Wolff, M. J., Christensen, P. R., Smith, M. D., Pearl, J. C., Conrath, B. J., and Wilson, R. J. (2000). An intercomparison of ground-based millimeter, MGS TES, and Viking atmospheric temperature measurements: Seasonal and interannual variability of temperatures and dust loading in the global Mars atmosphere. *J. Geophys. Res.: Planets*, *105*(E4), 9553–9571. https://doi.org/10.1029/1999JE001089

de Vaucouleurs, G. H. (1954). Physics of the planet Mars; an introduction to areophysics. *London*. Retrieved from https://ui.adsabs.harvard.edu/abs/1954ppmi.book.....D

Edwards, C. S., Nowicki, K. J., Christensen, P. R., Hill, J., Gorelick, N., and Murray, K. (2011). Mosaicking of global planetary image datasets: 1. Techniques and data processing for Thermal Emission Imaging System (THEMIS) multi-spectral data. *J. Geophys. Res.: Planets*, *116*(E10), E10008. https://doi.org/10.1029/2010JE003755

Fenton, L. K., Geissler, P. E., and Haberle, R. M. (2007). Global warming and climate forcing by recent albedo changes on Mars. *Nature*, *446*(7136), 646–649. https://doi.org/10.1038/nature05718

Geissler, P. E. (2005). Three decades of Martian surface changes. *J. Geophys. Res.: Planets*, *110*(E2), E02001. https://doi.org/10.1029/2004JE002345

Geissler, P. E., Fenton, L. K., Enga, M. T., and Mukherjee, P. (2016). Orbital monitoring of Martian surface changes. *Icarus*, *278*, 279–300. https://doi.org/10.1016/j.icarus.2016.05.023

Guzewich, S. D., Fedorova, A. A., Kahre, M. A., and Toigo, A. D. (2020). Studies of the 2018/Mars year 34 planet-encircling dust storm. *J. Geophys. Res.: Planets*, *125*(12), e2020JE006700. https://doi.org/10.1029/2020JE006700

Haberle, R. M., Clancy, R. T., Forget, F., Smith, M. D., and Zurek, R. W. (2017). *The Atmosphere and Climate of Mars*. Cambridge: Cambridge University Press. https://doi.org/10.1017/9781139060172

Herkenhoff, K. E., and Murray, B. C. (1990). Color and albedo of the south polar layered deposits on Mars. *J. Geophys. Res.: Solid Earth*, *95*(B2), 1343–1358. https://doi.org/10.1029/JB095iB02p01343

Herkenhoff, K. E., and Plaut, J. J. (2000). Surface ages and resurfacing rates of the polar layered deposits on Mars. *Icarus*, *144*(2), 243–253. https://doi.org/10.1006/icar.1999.6287

Hernández-Bernal, J., Sánchez-Lavega, A., del Río-Gaztelurrutia, T., Hueso, R., Cardesín-Moinelo, A., Ravanis, E. M., De Burgos-sierra, A., Titov, D., and Wood, S. (2019). The 2018 Martian global dust storm over the south polar region studied with MEx/VMC. *Geophys. Res. Lett.*, *46*(17-18), 10330–10337. https://doi.org/10.1029/2019GL084266

James, P. B., Cantor, B. A., and Davis, S. (2001). Mars Orbiter Camera observations of the Martian south polar cap in 1999-2000. *J. Geophys. Res.: Planets*, *106*(E10), 23635–23652. https://doi.org/10.1029/2000JE001313

James, P. B., Bonev, B. P., and Wolff, M. J. (2005). Visible albedo of Mars' south polar cap: 2003 HST observations. *Icarus*, *174*(2), 596–599. https://doi.org/10.1016/j.icarus.2004.08.024

James, P. B., Thomas, P. C., Wolff, M. J., and Bonev, B. P. (2007). MOC observations of four Mars year variations in the south polar residual cap of Mars. *Icarus*, *192*(2), 318–326. https://doi.org/10.1016/j.icarus.2007.07.014

Kahre, M. A., Murphy, J. R., Newman, C. E., Wilson, R. J., Cantor, B. A., Lemmon, M. T., and Wolff, M. J. (2017). The Mars dust cycle. In R. M. Haberle, et al. (Eds.), *The Atmosphere and Climate of Mars* (pp. 295-337). Cambridge: Cambridge University Press. https://doi.org/10.1017/9781139060172.010

Khuller, A. R., Christensen, P. R., and Warren, S. G. (2021). Spectral albedo of dusty Martian H_2O snow and ice. *J. Geophys. Res.: Planets*, *126*(9), e2021JE006910. https://doi.org/10.1029/2021JE006910

Kieffer, H. H., Martin, T. Z., Peterfreund, A. R., Jakosky, B. M., Miner, E. D., and Palluconi, F. D. (1977). Thermal and albedo mapping of Mars during the Viking primary mission. *J. Geophys. Res.*, *82*(28), 4249–4291. https://doi.org/10.1029/JS082i028p04249

Kieffer, H. H. (1979). Mars south polar spring and summer temperatures: a residual CO_2 frost. *J. Geophys. Res.: Solid Earth*, *84*(B14), 8263–8288. https://doi.org/10.1029/JB084iB14p08263

Kieffer, H. H., Titus, T. N., Mullins, K. F., and Christensen, P. R. (2000). Mars south polar spring and summer behavior observed by TES: seasonal cap evolution controlled by frost grain size. *J. Geophys. Res.: Planets*, *105*(E4), 9653–9699. https://doi.org/10.1029/1999JE001136

Kinch, K. M., Sohl-Dickstein, J., Bell III, J. F., Johnson, J. R., Goetz, W., and Landis, G. A. (2007). Dust deposition on the Mars Exploration Rover Panoramic Camera (Pancam) calibration targets. *J. Geophys. Res.: Planets*, *112*(E6), E06S03. https://doi.org/10.1029/2006JE002807

Labs, D., and Neckel, H. (1968). The radiation of the solar photosphere from 2000 Å to 100 μm. *Z. Astrophys.*, *69*, 1.

Langevin, Y., Poulet, F., Bibring, J. P., Schmitt, B., Douté, S., and Gondet, B. (2005). Summer evolution of the North Polar Cap of Mars as observed by OMEGA/Mars express. *Science*, *307*(5715), 1581–1584. https://doi.org/10.1126/science.1109438

Langevin, Y., Bibring, J. P., Montmessin, F., Forget, F., Vincendon, M., Douté, S., Poulet, F., and Gondet, B. (2007). Observations of the south seasonal cap of Mars during recession in 2004-2006 by the OMEGA visible/near-infrared imaging spectrometer on board Mars Express. *J. Geophys. Res.: Planets*, *112*(E8), E08S12. https://doi.org/10.1029/2006JE002841

Leighton, R. B., and Murray, B. C. (1966). Behavior of carbon dioxide and other volatiles on Mars. *Science*, *153*(3732), 136–144. https://doi.org/10.1126/science.153.3732.136

Malin, M. C., Calvin, W. M., Cantor, B. A., Clancy, R. T., Haberle, R. M., James, P. B., Thomas, P. C., Wolff, M. J., Bell, J. F., and Lee, S. W. (2008). Climate, weather, and north polar observations from the Mars Reconnaissance Orbiter Mars Color Imager. *Icarus*, *194*(2), 501–512. https://doi.org/10.1016/j.icarus.2007.10.016

Martínez, G. M., Renno, N. O., and Elliott, H. M. (2012). The evolution of the albedo of dark spots observed on Mars polar region. *Icarus*, *221*(2), 816–830. https://doi.org/10.1016/j.icarus.2012.09.008

Montmessin, F., Haberle, R. M., Forget, F., Langevin, Y., Clancy, R. T., and Bibring, J. P. (2007). On the origin of perennial water ice at the south pole of Mars: A precession-controlled mechanism?. *J. Geophys. Res.: Planets*, *112*(E8), E08S17. https://doi.org/10.1029/2007JE002902

Morgan, F., Seelos, F., Murchie, S., and the CRISM Team. (2009). CRISM Data Users' Workshop CAT Tutorial. Retrieved from https://pds-geosciences.wustl.edu/missions/mro/CRISM_Workshop_090322_CAT_MFM.pdf

Murchie, S., Arvidson, R., Bedini, P., Beisser, K., Bibring, J. P., Bishop, J., Boldt, J., Cavender, P., Choo, T., … Wolff, W. (2007). Compact Reconnaissance Imaging Spectrometer for Mars (CRISM) on Mars Reconnaissance Orbiter (MRO). *J. Geophys. Res.: Planets*, *112*(E5), E05S03. https://doi.org/10.1029/2006JE002682

Paige, D. A., and Ingersoll, A. P. (1985). Annual heat balance of Martian polar caps: Viking observations. *Science*, *228*(4704), 1160–1168. https://doi.org/10.1126/science.228.4704.1160

Pollack, J. B., Greenberg, E. H., and Sagan, C. (1967). A statistical analysis of the Martian wave of darkening and related phenomena. *Planet. Space Sci.*, *15*(5), 817–824. https://doi.org/10.1016/0032-0633(67)90117-1

Rice, M. S., Reynolds, M., Studer-Ellis, G., Bell, J. F., Johnson, J. R., Herkenhoff, K. E., Wellington, D., and Kinch, K. M. (2018). The albedo of Mars: Six Mars years of observations from Pancam on the Mars Exploration Rovers and comparisons to MOC, CTX and HiRISE. *Icarus*, *314*, 159–174. https://doi.org/10.1016/j.icarus.2018.05.017

Sánchez-Lavega, A., del Río-Gaztelurrutia, T., Hernández-Bernal, J., and Delcroix, M. (2019). The onset and growth of the 2018 Martian global dust storm. *Geophys. Res. Lett.*, *46*(11), 6101–6108. https://doi.org/10.1029/2019GL083207

Schaller, E. L., Murray, B., Pathare, A. V., Rasmussen, J., and Byrne, S. (2005). Modification of secondary craters on the Martian South Polar Layered Deposits. *J. Geophys. Res.: Planets*, *110*(E2), E02004. https://doi.org/10.1029/2004JE002334

Singh, D., and Flanner, M. G. (2016). An improved carbon dioxide snow spectral albedo model: Application to Martian conditions. *J. Geophys. Res.: Planets*, *121*(10), 2037–2054. https://doi.org/10.1002/2016JE005040

Smith, M. D., Conrath, B. J., Pearl, J. C., and Christensen, P. R. (2002). Thermal emission spectrometer observations of Martian planet-encircling dust storm 2001A. *Icarus*, *157*(1), 259–263. https://doi.org/10.1006/icar.2001.6797

Smith, M. D. (2019). THEMIS observations of the 2018 Mars global dust storm. *J. Geophys. Res.: Planets*, *124*(11), 2929–2944. https://doi.org/10.1029/2019JE006107

Szwast, M. A., Richardson, M. I., and Vasavada, A. R. (2006). Surface dust redistribution on Mars as observed by the Mars Global Surveyor and Viking orbiters. *J. Geophys. Res.: Planets*, *111*(E11), E11008. https://doi.org/10.1029/2005JE002485

Tanaka, K. L., Skinner, J. A., Dohm, J. M., Iii, R. P. I., Kolb, E. J., Fortezzo, C. M., Platz, T., Michael, G. G., and Hare T. M. (2014). *Geologic map of Mars* (No. 3292). *Scientific Investigations Map*. Reston: U.S. Geological Survey. https://doi.org/10.3133/sim3292

Thomas, P., and Veverka, J. (1979). Seasonal and secular variation of wind streaks on Mars: An analysis of Mariner 9 and Viking data. *J. Geophys. Res.: Solid Earth*, *84*(B14), 8131–8146. https://doi.org/10.1029/JB084iB14p08131

Titus, T. N., Kieffer, H. H., and Christensen, P. R. (2003). Exposed water ice discovered near the South Pole of Mars. *Science*, *299*(5609), 1048–1051. https://doi.org/10.1126/science.1080497

Vincendon, M., Audouard, J., Altieri, F., and Ody, A. (2015). Mars Express

measurements of surface albedo changes over 2004-2010. *Icarus, 251*, 145-163. https://doi.org/10.1016/j.icarus.2014.10.029

Viviano, C. E., Seelos, F. P., Murchie, S. L., Kahn, E. G., Seelos, K. D., Taylor, H. W., Taylor, K., Ehlmann, B. L., Wiseman, S. M., … Morgan, M. F. (2014). Revised CRISM spectral parameters and summary products based on the currently detected mineral diversity on Mars. *J. Geophys. Res.: Planets*, *119*(6), 1403–1431. https://doi.org/10.1002/2014JE004627

Viviano, C. E., Murchie, S. L., Seelos, F. P., Seelos, K. D., and Cartwright, S. F. A. (2022). Strategies for mapping ice on mars using CRISM VNIR wavelengths. In *53rd Lunar and Planetary Science Conference*. The Woodlands: LPI.

Warren, S. G., Wiscombe, W. J., and Firestone, J. F. (1990). Spectral albedo and emissivity of CO_2 in Martian polar caps: Model results. *J. Geophys. Res.: Solid Earth*, *95*(B9), 14717–14741. https://doi.org/10.1029/JB095iB09p14717

Wolkenberg, P., Giuranna, M., Smith, M. D., Grassi, D., and Amoroso, M. (2020). Similarities and differences of global dust storms in MY 25, 28, and 34. *J. Geophys. Res.: Planets*, *125*(3), e2019JE006104. https://doi.org/10.1029/2019JE006104

Zurek, R. W., and Smrekar, S. E. (2007). An overview of the Mars Reconnaissance Orbiter (MRO) science mission. *J. Geophys. Res.: Planets*, *112*(E5), E05S01. https://doi.org/10.1029/2006JE002701